Effect of lanthanum doping on the structure and optical properties of nanocrystalline vanadium pentoxide films prepared by sol–gel method

M. M. Abdelrazek[1] · Ahmed E. Hannora[2] · Rasha M. Kamel[3] · Ibrahim Morad[1] · M. M. El-Desoky[1]

Abstract

The structural and optical properties of lanthanum oxide doped nanocrystalline vanadium pentoxide films with the chemical composition $xLa_2O_3\text{-}(1\text{-}x)V_2O_5.nH_2O$ (where $x = 0.25$, 0.50 and 1.0 mol%) prepared by sol–gel method were studied. The XRD analysis also revealed that the (002) line is noticeable in the pure film and gets sharper by the addition of Lanthanum, which indicates a layer of intercalation between the vanadium layers. The average crystallite size decreased with increasing Lanthanum content from 4.45 nm to 3.57 nm. By using double-beam UV–VIS spectrophotometers, the optical properties were studied by measuring the absorption, reflectance and transmittance of the prepared films. Some optical parameters like absorption coefficient α, dispersion energy parameters, refractive index n, optical band gap E_{op} for various transition mechanisms, real parts and imaginary part of the dielectric constants and effective mass were calculated. The absorption coefficient slightly increases with increasing La content, which can be attributed to the increasing of lattice distortion as a result of crystallite size increasing as indicated in the XRD. The transition mechanism was found to be indirect allowed type with optical band gap E_{op} increasing relative to the La content. By assuming hydrogen like model, the carrier's contents N were deduced. The absorption spectrum behavior in visible and UV region suggests a promising solution for solar cells and optical-electronic applications.

Keywords Nanocrystalline vanadium pentoxide films · Lanthanum oxide · sol–gel · Optical properties

✉ M. M. El-Desoky
mmdesoky@gmail.com; mmdesoky@suezuniv.edu.eg

1   Department of Physics, Faculty of Science, Suez University, Suez 43518, Egypt

2   Department of Science and Engineering Mathematics, Faculty of Petroleum and Mining Engineering, Suez University, Suez 43518, Egypt

3   Chemistry Department, Faculty of Science, Suez University, Suez 43518, Egypt

1 Introduction

In our modern life, optically transparent electronics are main component in our devices. Vanadium pentoxide is one of the promising materials for such applications due to its unique optical properties (Prociow et al. 2011). The unique structure of vanadium pentoxide sol–gel, $V_2O_5.nH_2O$, proposed by Aldebert (1983) as layered structure host material allowing water molecules to intercalate between its layers. The structural model for vanadium pentoxide, V_2O_5, as proposed by T. Yao and Y. Oka (1997) has a lamellar structure, as shown in Figs. 1 and 2, respectively which is a distorted orthorhombic structure with flat-sheet like shape, is believed to be the main cause for its unique optical properties and forms a promising base for wide range of combinations through doping materials which directly changes the structural and optical properties.

Because of this layered structure, Vanadium pentoxide can be intercalated by many transitional metals which directly alter or add physical properties (Mohaghegh et al. 2019). For example, Srilakshmi et al. (2019), studied the effect of Ti and Zr doping on vanadium pentoxide absorption edge and found that Ti causes red shifting while Zr causes blue shifting
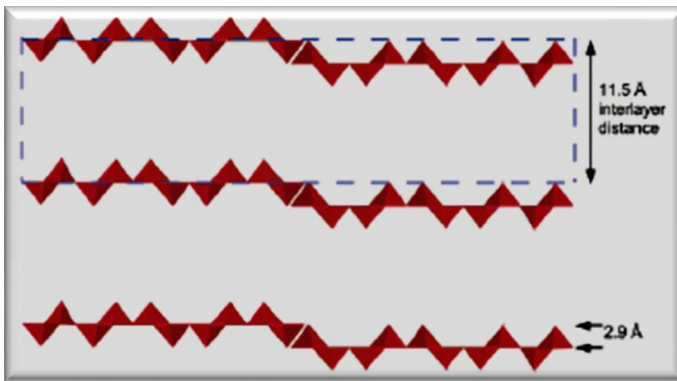

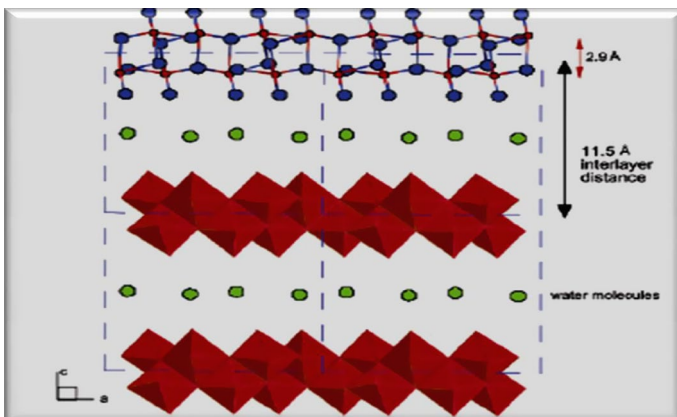**Fig. 1** Structural model for theV$_2$O$_5$ xerogel, proposed by Aldebert et al.

Fig. 2 Structural model for theV$_2$O$_5$ xerogel, proposed by Yao et al.

of the absorption edge. They also found that the band gap can be reduced from 2.2 eV for pure V_2O_5 to 1.96 eV for Ti-doped V_2O_5 which is a promising route for photovoltaic and photoluminescence applications. Vanadium pentoxide is also a promising material when doped with some halogen elements for optical–electrical and electrochromic applications. For example, Abyazisani, et al. (2015), studied the effect of fluorine doping on enhancing the electrochromic and optical properties of Vanadium pentoxide films. The band gap for vanadium pentoxide can also be altered depending on the preparation and treatment method. Etemadi et al. (2017), were able to reduce the band gap Cerium doped V_2O_5 films prepared by sol–gel method from 2.68 to 2.28 eV by increasing annealing temperature.

Rare-earth elements "sometimes called lanthanides", and rare earth doped materials have been widely researched due to their diverse optical applications in the fields of solar energy, up-conversion, lasers, color displays, optical amplifiers and temperature sensors, etc. (Monteiro et al. 2013; Lozano et al. 2013; Maaoui et al. 2016; Mohanty and Rai 2014; Annapoorani et al. 2016; Maheshvaran et al. 1079; Seshadri et al. 2014; Sajna et al. 2015; Maqbool et al. 2015). Lanthanum is the first element in the lanthanide group with electronic configuration [Xe] $5d^1 6s^2$ is one of the most common rare earth elements occupying about 14.1% of total rare earth resources (Zhao et al. 2011) which makes it economically suitable for optical application industries.

One of the most preferred techniques for synthetizing doped optical materials is sol–gel method where a colloidal solution "Sol" is gradually turned into a "gel" form including both solid and liquid phases. Sol–gel method has relatively lower in-process temperature, less impurities and higher homogeneity with uniform particle size at the nanometer level compared to most of chemical solid-state methods (Klein 2013; Al-Assiri et al. 2010a). Sol-gels also enable easy synthesis of thin films via multiple techniques as thin film samples are most suitable for investigating optical properties. The utilization of vanadium pentoxide gels opens a promising window for efficient optical and electronic devices (Ramana et al. 1997; Bahgat et al. 2011; Mady et al. 2012) due to its semiconducting properties raised from its electron transfer between V^{4+} and V^{5+} ions (Wright 1984; Takeda et al. 1996). The optical transmittance spectrum of V_2O_5 sol–gel has a characteristic absorption band at a wavelength of about 500 nm with nearly stable transmittance of about 75% in the visible region which makes it a good candidate for solar cell applications.

In our study, we focused on lanthanum in the form of lanthanum oxide La_2O_3 which intercalate between vanadium pentoxide layers during the formation of sol–gel as illustrated in Fig. 3. This intercalation is expected to alter the optical properties of vanadium pentoxide gels.

In this work we aim to study the influence of lanthanum oxide on the nano-structural and optical properties in the visible and near infrared regions of vanadium pentoxide nanocrystalline films for solar cells and opto-electronic applications. The lanthanum doped vanadium pentoxide films in the form of x La_2O_3-$(1+x)V_2O_5$.nH_2O (where x = 0.25, 0.50 and 1.0 mol%) are prepared via sol–gel technique.

2 Experimental

Lanthanum oxide in the form of La_2O_3 powder and Vanadium pentoxide in the form of V_2O_5 powder were purchased from Sigma Aldrich with 99.9% purity. For the present investigation, three different samples of x La_2O_3-$(1+x)V_2O_5$.nH_2O were prepared (x = 0.25, 0.50 and 1.0 mol%) as exceeding the La content to more than 1.0 mol%, the gelation was not forming. Then, for each sample, added the doping weight of La_2O_3

Fig. 3 Lanthanum Oxide
structure
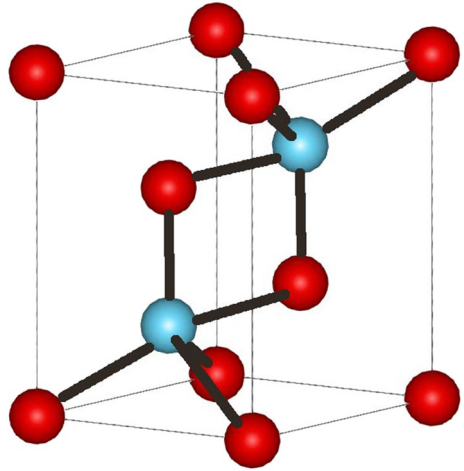
powder to 30 ml of 25% H_2O_2 then, adding 1 g of pure V_2O_5 while stirring. During the stirring, an exothermic reaction starts and lanthanum oxide starts intercalating within the vanadium pentoxide layers and gel starts to form within 30 min of medium stirring. Nanocrystalline films made by dip-coating technique were obtained for each concentration. The coating process starts at a fixed time of 5 h from reaction for all concentrations to assure homogenous viscosity. The coating is done at room temperature in a single coating layer with an average withdrawn speed of 15 mm/s.

All prepared samples were characterized by XRD using SIEMENS D5000 X-ray Diffractometer (monochromatic CuKα radiation source of $\lambda = 1.5406$ Å). The diffraction data were plotted for 2θ between 5 and 60 degrees with a resolution of 0.05. The resulted graphs were processed and compared with international database by pattern recognition software "X'Pert HighScore®" which identifies the existing planes, crystal structure and the and interplanar spacing. Furthermore, graph analysis software, Origin ®, was used to analyze the peaks and their full width half maximum (FWHM) to calculate the average crystallite size using Scherrer method for each La concentartin. HRTEM for present samples were analyzed by JEOL JEM-2100 HRTEM at various magnifications. For each sample, the general structure, crystallite size and EDX was analyzed. For the optical properties we used METASH 9000 UV/VIS spectrophotometer operating from UV region ($\lambda = 190$ nm) to IR region ($\lambda = 1100$ nm). The prepared samples were tested for optical transmittance (T), absorption (A) and reflectance (R) at room temperature. Slit width or signal amplification gain is controlled automatically to adjust the base line before any series of measurements. Then, film thickness (t), was obtained using SWANEPOEL method (Sánchez-González et al. 2006; Li et al. 2009; Caglar et al. 2006) and optical limiting estimating the thickness from the cut-off intensity of a 650 nm laser. Other optical parameters for different doping contents were investigated including optical direct and indirect band gap, Urbach activation energy, the dissipation factor (tan δ), surface energy loss, volume energy loss, dispersion energy parameters and real ε' and imaginary ε'' parts of the dielectric constant (Fig. 4).

3 Results and discussion

3.1 XRD Analysis

The X-ray diffraction for the prepared films are plotted in Fig. 5. By running analysis for resulted XRD plot using XRD-analysis software, it was found thet card number 00–040–1296 or/ (JCPDS 40–1296) orthorhombic vanadium pentoxide xerogel crystal system is a good match (Al-Assiri et al. 2010a; Li et al. 2014). From Fig. 5, we notice a maximum intensity peak corresponding to (001) plane appearing at 2Θ of 6.8~7.2 with no noticable change in Bragg's angle by the addition of La%. Other peaks related to (002), (003), (004) and (005) are appearing for all La% contents also at the same Bragg's angle compared to pure sample. However, for 0.25%La, peak (003) is noticed with ~1 (2θ-degrees) shift to lower Bragg's angle compared to pure sample. Peak (002) is noticeable in the pure film and gets sharper by the addition of Lanthanum with sharpest peak in 0.50%La, which indicates a layer of intercalation between the vanadium layers. Peak (002) is also tending to be sharper by the addition of lanthanum which can be explained by the formation of lanthanum vanadium oxide $La0.35O_5V_2$ with main peak at (002) which is a good match with card number 00–050–0456. Other peaks for Lanthanum oxide is expected to be very week due to relatively low doping concentration (max 1 mol%) relative to 99 mol% Vanadium pentoxide.

The intinsity of the main peak (001) is found to be decreasing with the addition of La% which indicates level of intercalation affecting the crystallite size. From XRD analysis, the obtained nanocrystalline films were found to be highly orientated nanocrystals with their c-axis normal to the substrate surface (Bahgat et al. 2005).

Texture coffecient (TC) is an important structural parameter to assure the implementation stabilty of the prepared materials (Mrabet et al. 2016). To confirmthe orintation, TC indicating the prefered maximum orintation along diffraction planes was obtained by the following equation using the XRD data (Fang et al. 2014)

$$TC_{(hkl)} = \frac{I(hkl)/I_o(hkl)}{N^{-1} \sum I(hkl)/I_o(hkl)} \tag{1}$$

where *I(hkl)* is the measured intensity from XRD for each peak, $I_0(hkl)$ is the corresponding intensity for each plane from JCPDS 40–1296 card and N is the number of diffraction peaks observed in the XRD pattern.The texture coffecient (TC) for different La contents is illustrated in Fig. 6. From the figure, palnes (001) and (004) showing TC > 1 which indicates that the film growth is occuring in a preffered orientation toword c-axis. However, TC
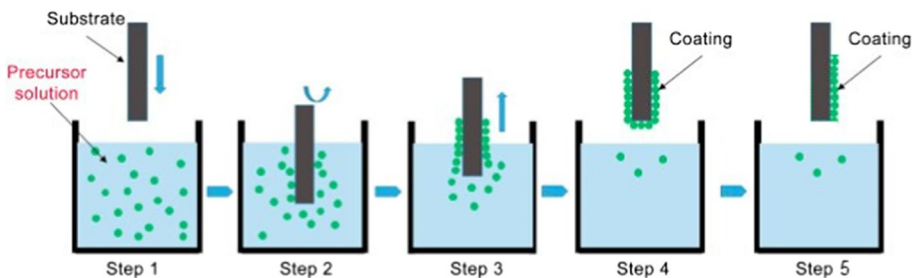

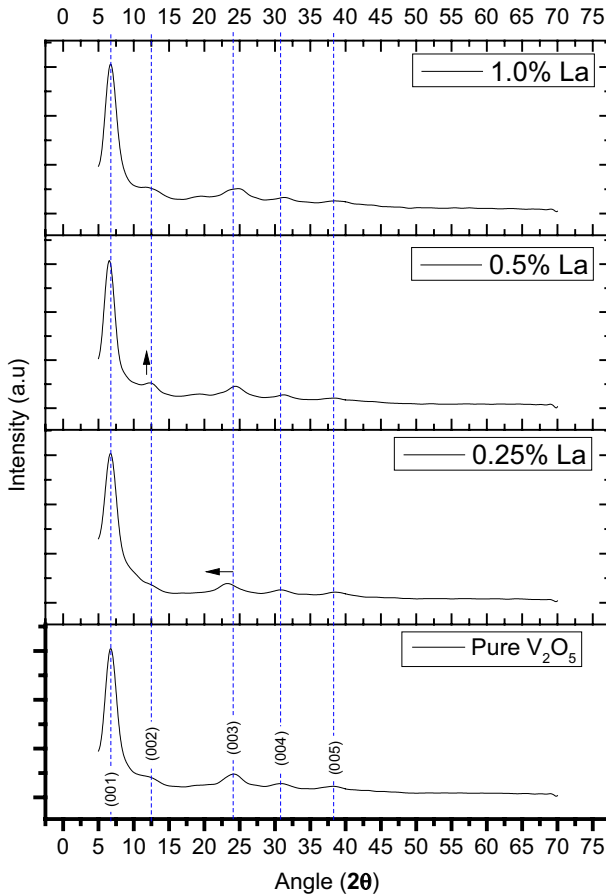**Fig. 4** Dip coating illustration

Fig. 5 Room-temperature XRD for different La oxide content in the relevant angles (2θ)

values for all peaks are not very sensitive to the doping concentration. Nevertheless, plane (002) has maximum TC value for 0.50% La which is expected from the sharp peak in XRD figure.

The average crystallite size (D) of nanocrystalline films was calculated by Debye-Scherer's equation, Eq. (2)

$$D = \frac{k\lambda}{\beta COS\theta} \tag{2}$$

where k ~1, λ = 1.5406 Å for Cu (Kα), β is the full width at half maximum (FWHM) in radians and θ is Bragg angle (Kaelble 1967). We used the Gauss fitting method from Origin® software for the main peak (001) to calculate the crystallite size. Table 1 contains the calculated crystallite size. The average crystallite size decreased with increasing Lanthanum content from 4.45 nm to 3.57 nm as indicated in Fig. 7. This decrease in average crystallite size is also noticeable from the decrease in intensity of XRD peaks especially main peak of plan (001). Also, the decrease can be explained by assuming that increasing doping concentration increases the substitution level of V^{5+} (ionic radius = 68 pm) by La^{3+}
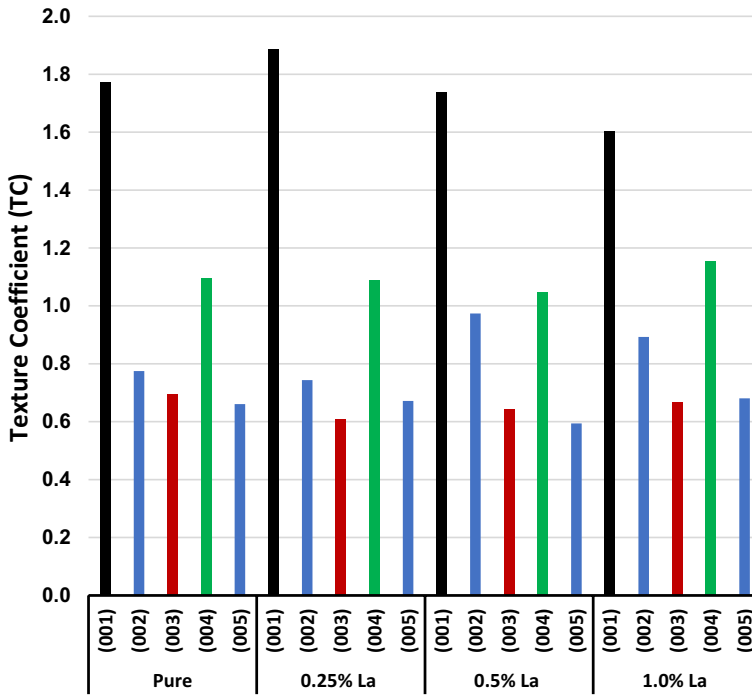
Fig. 6 Texture Coefficient (TC)

Table 1 Crystallite size in (nm) calculated, micro-strain (ζ) and dislocation density (δ) for different La oxide content

Sample	[La/V$_2$O$_5$] mol ratio	Average D (nm)	$\zeta \times 10^{-3}$	$\delta \times 10^{+15}$
Pure V$_2$O$_5$	0	4.45	36.90	50.54
0.25% La	0.0025	3.85	37.90	67.39
0.50% La	0.005	3.81	43.12	69.05
1.00% La	0.01	3.57	52.93	78.66

(ionic radius = 117 pm) which increases the internal stress and hence increasing the lattice distortion level which inhibits the crystallites growth of V$_2$O$_5$ and reduces its crystallinity (Fang et al. 2014; Chikhale et al. 2014).

The effect of La doping on the micro-strains (ζ) are calculated by the following equation:

$$\zeta = \frac{\beta''}{4 \tan \theta} \tag{3}$$

where ζ is the micro-strain in radians, β" is the full width at half maximum (FWHM) of (001) peak in radians and θ is the Bragg's angle in degrees. The calculated values for micro-strain (ζ) are tabulated in Table 1 and shows values increasing with the addition of Lanthanum which is related to the increase of internal stress.
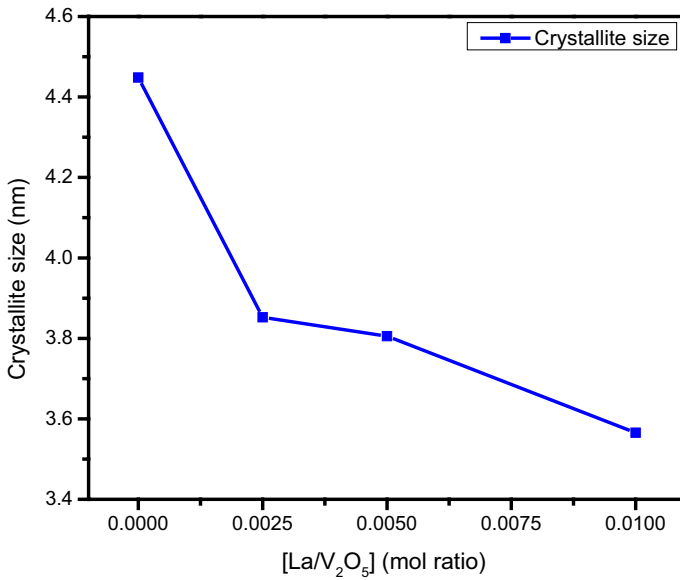
Fig. 7 Crystallite size for different La content

Dislocation level resulting from the grain growth is estimated from dislocation density (δ) which defined as the length of dislocation lines per unit surface (lines/m^2) (Mrabet et al. 2016). The dislocation density (δ) is calculated from the following equation (Amlouk et al. 2009):

$$\delta = \frac{1}{D} \tag{4}$$

where D is the average crystallite size, dislocation density (δ) is calculated for different La% contents and listed in Table 1 and shows increase of dislocation density with the addition of lanthanum which is expected due the decrease in average crystallite size.

3.2 HRTEM

The structural information of the prepared samples with La of 1.0 mol% are obtained from high resolution transmission electron microscope (HRTEM) observation. Figure 8a show HRTEM general structure at 200 nm scale shows vanadium layers. Figure 8b taken at 50 nm scale showing particle size measured from ~9 to ~19 nm which is higher than average crystallite size measured from XRD. Figure 8c shows clear lattice fringes implying high nanosheet crystallinity. It brings out a lattice spacing of ~0.36 nm which is related to (003) plane which correspond to c-axis and which agrees with calculated d-spacing from X-ray diffraction of (003) plane (0.345 nm). The inset of Fig. 9 shows the corresponding selected area electron diffraction (SAED)
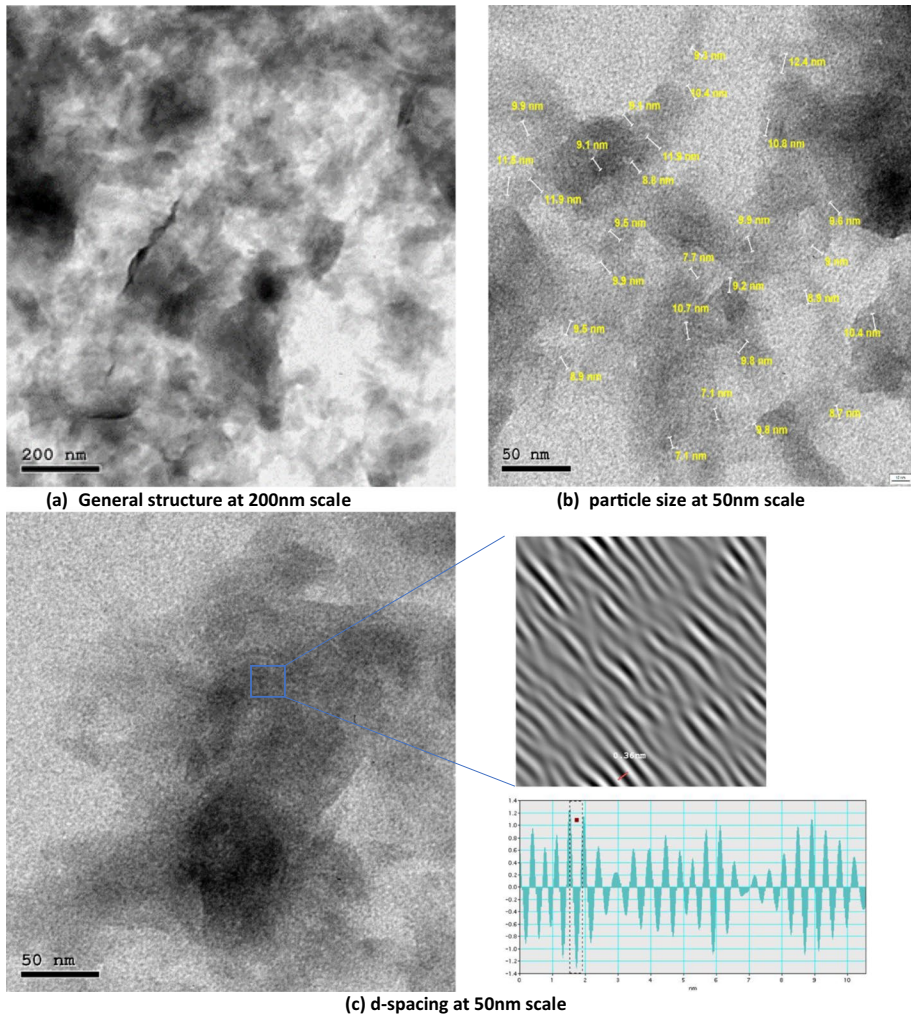
(a) General structure at 200nm scale

(b) particle size at 50nm scale

(c) d-spacing at 50nm scale

Fig. 8 a HRTEM at 200 nm scale **b** measured particle size at 100 nm scale **c** d-spacing at 50 nm scale

pattern of 1.0 mol%.The diffraction spots match in good agreement with the JCPDS file (40–1296) (Nagaraju et al. 2014).

3.3 Film thickness

The film thickness (t) was calculated using SWANEPOEL method (Sánchez-González et al. 2006; Li et al. 2009; Caglar et al. 2006). This method calculates the thickness by analysing the envelop of the transmittance spectrum and perform theoretical calculations which takes into account the interference effects. Where (t) is film thickness, (n) is a complex refractive index and (k) is extinction coefficient that is expressed in the terms of the absorption coefficient (α). The substrate has a thickness of seVeral orders
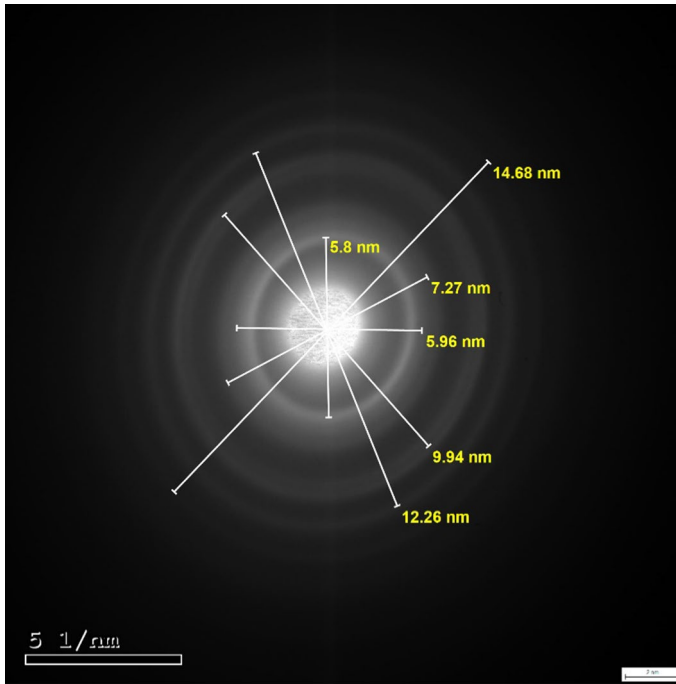
Fig. 9 X-ray diffraction from HRTEM

of magnitude larger than that of the film and a refractive index (s). As the interference phenomena between the wave fronts generated at the two interfaces (air and substrate), defines the sinusoidal behavior of the curves' transmittance vs. wavelength of light (Aristizábal and Mikan 2016). Using Origin® signal processing tools to draw curve envelop T_{max} and T_{min} are the transmissivity envelope curve maximum and the minimum of the normal incidence transmitted spectrum where N is defined according to the following equation:

$$N = \frac{1}{2}\left(1 + S^2\right) + 2S\left(T_{max} - T_{\min)}\right)/\left(T_{max} * T_{\min)}\right) \tag{5}$$

and s is the refractive index of glass substrate (1.52). The thickness (t) of the nanocrystalline films was calculated using as following:

$$t = \frac{\lambda_1 \lambda_2}{2\left(\lambda_1 N_2 - \lambda_2 N_1\right)} \tag{6}$$

where t is the film thickness, λ_1 and λ_2 are wavelengths corresponding to two adjacent interference peaks, and N_1 and N_2 defined by Eq. (5) for λ_1 and λ_2, respectively.

SWANEPOEL method is applied only to all samples with interference pattern in transmittance spectrum. Then, the optical limiting is measured for those samples by measuring the cut-off intensity of a 650 nm laser at a fixed distance to deduce a linear

Table 2 Film thickness for different La oxide content

Sample	Pure	0.25 mol%	0.50 mol%	1.00 mol%
[La/V$_2$O$_5$] mol ratio	0	0.0025	0.005	0.01
t (µm)	0.897	0.868	0.939	0.897

corelation between the cut-off intensity and film thikness. This linear relation is then used to deduces the thickness for samples with missing interference pattern.

Films thicknesses are evaluated according to Eq. (6) and listed in Table 2.

3.4 UV- visible spectroscopic analysis

The absorption, A, transmittance, T and reflectance, R, spectra were recorded at room temperature in wavelength ranging from 190 to 1100 nm as indicated in Fig. 10a, b and c, respectively. In Fig. 10a, for UV region 190 nm to 285 nm, the absorptivity is less than 5% relative to maximum value on the curve. For near UV and visible region, from 285 to 500 nm, the absorptivity is generally increasing with the addition of the La% but without any noticeable shift in wave lengths relative to the pure V$_2$O$_5$ sample. La with 0.50 mol% has heigher peak in this region which can be related to the sharp (002) peak appearing in XRD analysis and is veryfied by analysing the effective absorptivity $\hat{\alpha}$. This result of absorption in the UV–VIS region can be concidered as a promessing candidate for solar cell applications (Lee, et al. 2016; Roose, et al. 2016; Roose, et al. 2018). From 500 nm to IR region up to 1100 nm, La with 0.25 mol% shows the highest absorptivity. In Fig. 10b, the transmittance can also be divided into three regions, from 190 to 285 nm, the transmittance decreases with the increase of La% content but has the highest percentage in this region, while from 285 to 500 nm, the transmittance is very week and generally increasing with the increase of La%. For VIS-IR region, from 500 to 1100 nm, the transmittance is decreases from about 80% to about 40% with increasing La%. The lowest transmittance is recorded in La of 0.25 mol%. This property shows that transmittance for certain wavelengths can be controlled by the addition of La. Figure 10c, in two regions, from 190 nm up to 500 nm, the reflectance is very week. And from 500 nm up to 1100 nm, the reflectance decreases with the addition of La%. Overlapping behavior is noticed in the IR region from 900 to 1100 nm which is related to nano crystallinity of V$_2$O$_5$ (Abyazisani et al. 2015; Dultsev et al. 2006; Tashtoush and Kasasbeh 2013).

3.5 Studying absorption coefficient α and effective absorptivity $\hat{\alpha}$

The absorption coefficient (α) for the prepared samples was computed using the absorption data as per following equation (Islam and Podder 2009; Al-Qaisi 2013; Indolia and Gaur 2013; El-Desoky et al. 2018, 2020):

$$\alpha = \frac{2.303 * A\%}{\text{Thickness (t)}} \tag{7}$$

The result of (α) as a function of energy in (eV) for the prepared samples is plotted in Fig. 11.

Fig. 10 **a** absorption, A, **b** transmittance, T and **c** reflectance, R, spectra for different La oxide content
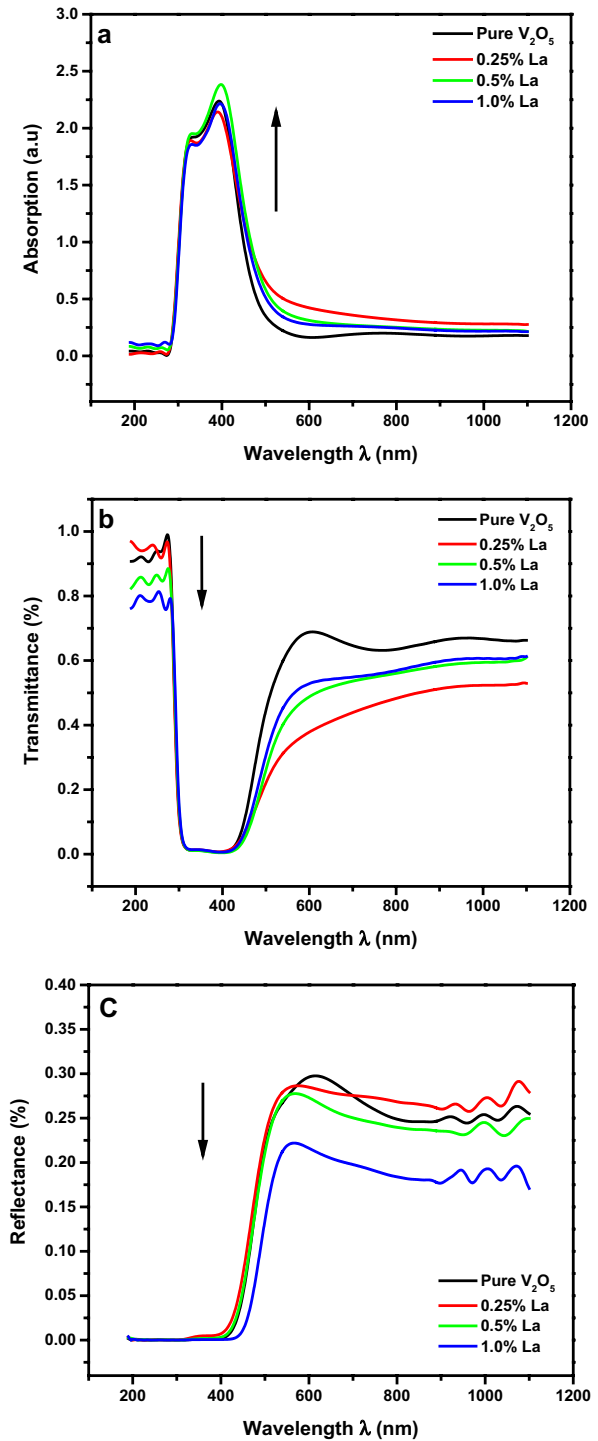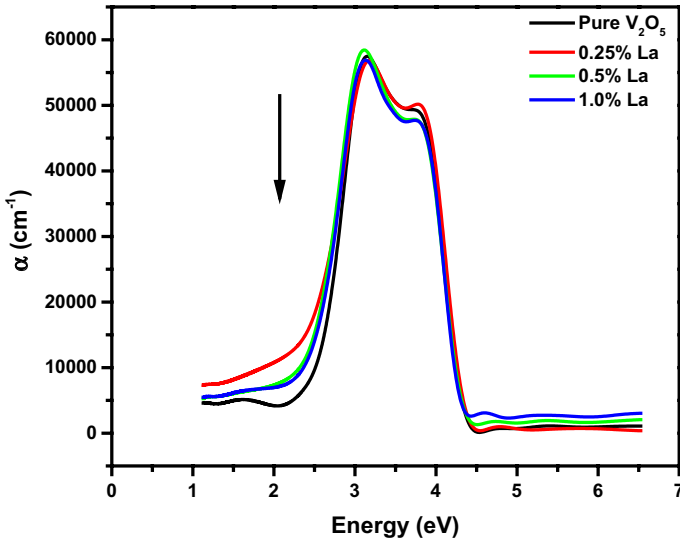
Fig. 11 Absorption coefficient (α) as a function of photon energy

The absorption coefficient generally increases with increasing La oxide content, which may be attributed to increase in lattice distortion owing to La oxide content due to the decrease of crystallinity.

The effective absorptivity $\hat{\alpha}$ is the mean absorbance weighted by $I(\lambda)AM_{1.5}$ (Mahmoud and Amlouk 2009; Lazzez et al. 2009) the solar standard spectral irradiance for visible light (400:750 nm), is an important optical parameter to evaluate the material for solar application. The effective absorptivity â is deduced from the following equation:
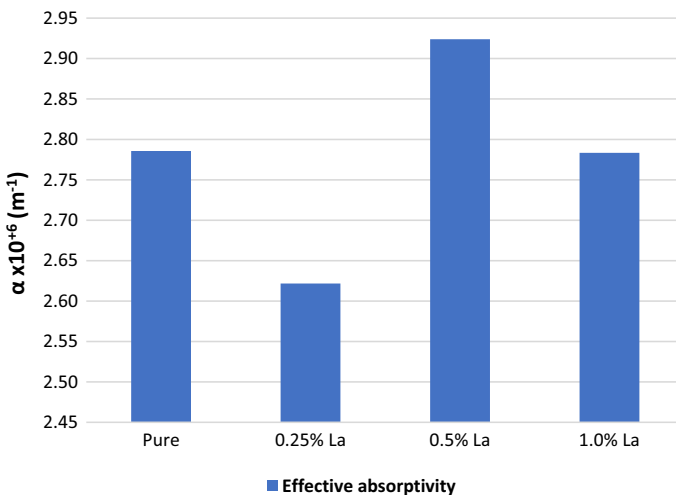

Fig. 12 Effective Absorptivity with different La doping

$$\hat{\alpha} = \frac{\int_{\lambda_{min}}^{\lambda_{max}} I(\lambda)_{AM1.5} X\alpha(\lambda)d\lambda}{\int_{\lambda_{min}}^{\lambda_{max}} I(\lambda)_{AM1.5}d\lambda} \quad (8)$$

where $\lambda_{min} = 400$ nm and $\lambda_{max} = 750$ nm. The calculated values for effective absorptivity $\hat{\alpha}$ are illustrated in Fig. 12. From the figure, it is clearly that doping with 0.50%La has enhanced the effective absorptivity in the visible light range which makes this doping level a promising candidate for solar cell applications. The relative increase in effective absorptivity for 0.50%La can be explained by the texture coefficient were plane (002) has maximum TC value in 0.50%La sample (Fig. 13).

3.6 Studying extinction coefficient k and refractive index n and

The obtained curves of absorption coefficient (α) for different La% contents were used to calculate the extinction coefficient k as plotted in Fig. 14. This parameter represents the lost light fraction via scattering and absorption per unit distance of the penetrated medium. Where α and k are related by Eq. (9) (Al-Assiri et al. 2010a; Tashtoush and Kasasbeh 2013; El-Desoky et al. 2018).

$$k = \frac{\alpha\lambda}{4\pi} \quad (9)$$

From the plotted curves, the extinction coefficient k generally increases with the addition of La% which was predicted as extinction coefficient k is directly proportional to the absorption coefficient (α) which also generally increased by the addition of La.
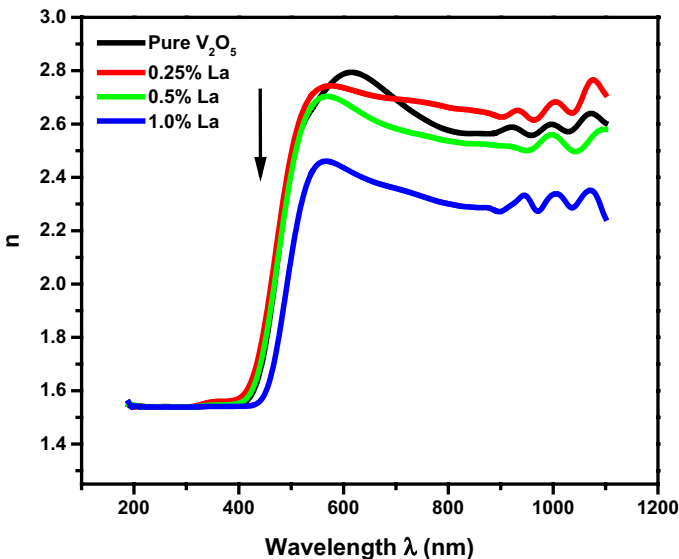

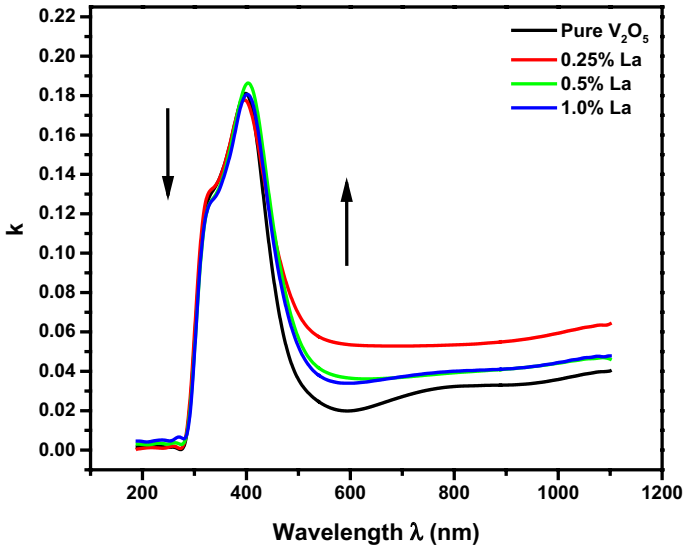**Fig. 13** Refractive index (n) as a function of wavelength λ

Fig. 14 Extinction coefficient (k) as a function of wavelength λ

From the reflectance curves, the refractive index n was calculated according to the following, assuming normal incidence and k < < n (El-Desoky et al. 2020, 2014), the reflection coefficient affecting the intensity of the radiation is given by Eq. (10) and illustrated in Fig. 13.

$$n = \frac{\left(1 + \sqrt{R}\right)}{\left(1 - \sqrt{R}\right)} \tag{10}$$

The refractive index of samples exhibit slightly variation with La oxide content which can be attributed to the increase of La oxide layers intercalated between V_2O_5 layers which as similar behavior for refractive index was found in other researches (Arefinia 2013; Schmiedova et al. 2017; Matkovic and Gajic 2013).

3.7 Dielectric constants and dissipation factor

To study the absorption band, we used the complex dielectric permittivity, $\varepsilon^* = \varepsilon' - i\ \varepsilon''$ where ε' and ε'' are respectively the real and imaginary parts of the dielectric constant.

The real ε' and imaginary ε'' parts of the dielectric constant are illustrated against wavelength in Fig. 15a and b respectively. Both real and imaginary parts of the dielectric constant are a function of refractive index n and extinction coefficient k, as per the following equations:
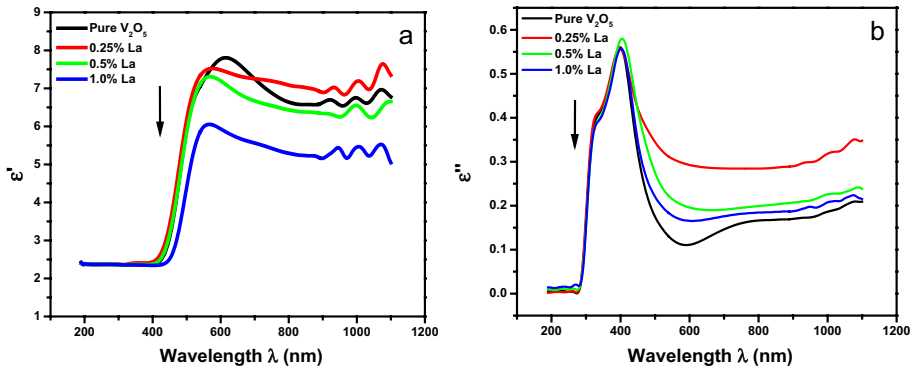
$$\text{Real part}, \varepsilon' = n^2 - K^2 \tag{11}$$

Fig. 15 **a** Real part of the dielectric(ε'), **b** Imaginary part of the dielectric (ε'') constant against wavelength λ
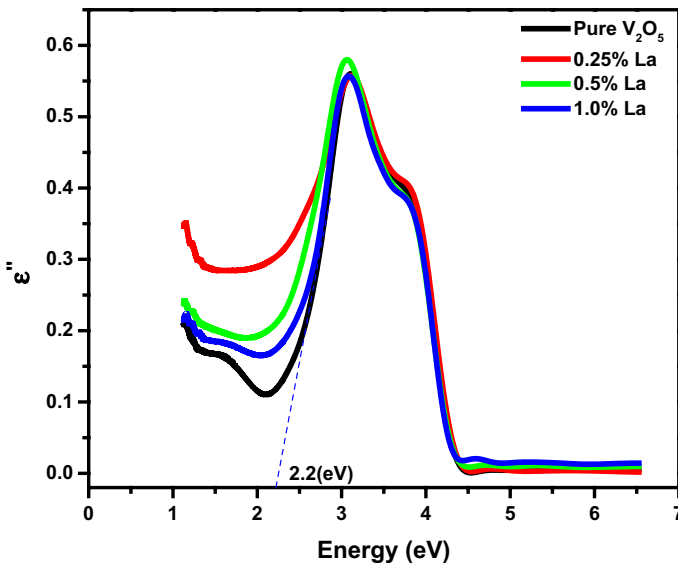

Fig. 16 Imaginary part of dielectric (ε'') as a function of photon energy

$$\text{Imaginary part, } \varepsilon'' = 2nK \tag{12}$$

The real part of the dielectric constant is similar to its behavior to the refractive index which was expected given the direct relation in Eq. (11). As for the imaginary part, it shows general increase after doping with La. Figure 16, shows the calculated values of ε'' as a function of E (eV) for prepared samples with different values of La doping. By extrapolating the linear parts to the intercept on the X-axis, the fundamental absorption band was estimated around ~2.2 eV which is related to wavelength ~564 nm in the visible spectrum.
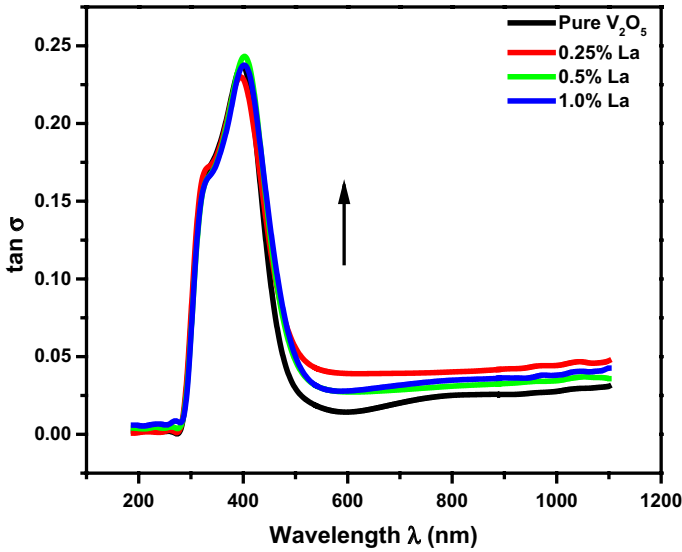
Fig. 17 The dissipation factor (tan δ) as a function of wavelength

By using the dielectric constant two parts ε' and ε'', the dissipation factor (tan δ), representing the rate of lost power for mechanical modes, such as an oscillation, can be calculated (El-Nahhas et al. 2012). Figure 17 shows the dissipation factor (tan δ) calculated by the following equation for various La% contents.

$$\tan \delta = \frac{\varepsilon''}{\varepsilon'} \tag{13}$$

The dissipation factor generally increased with La doping. It is clearly that dissipation factor (tan δ) will also behave like the imaginary part of the dielectric constant which is expected as indicated in Eq. (13).

3.8 Optical transition type and band gap (E_{op})

The optical band gap E_{op} is corresponding to the minimum energy required for photons to induce transition from the conduction band to valance band. There are four known mechanisms for optical energy transition (direct allowed, direct forbidden, indirect allowed and indirect forbidden).

Using the absorption coefficient α, the band gap can be calculated from Tauc's equation (Tashtoush and Kasasbeh 2013; Ghobadi 2013):

$$\alpha h\upsilon = \beta \left(h\upsilon - E_{op} \right)^{m} \tag{14}$$

where β is the band edge width parameter related to the quality of the film and m is a parameter representing the type of the optical transition as following and m depends on the nature of the optical transition (Al-Assiri et al. 2010a; Ghobadi 2013). On the other
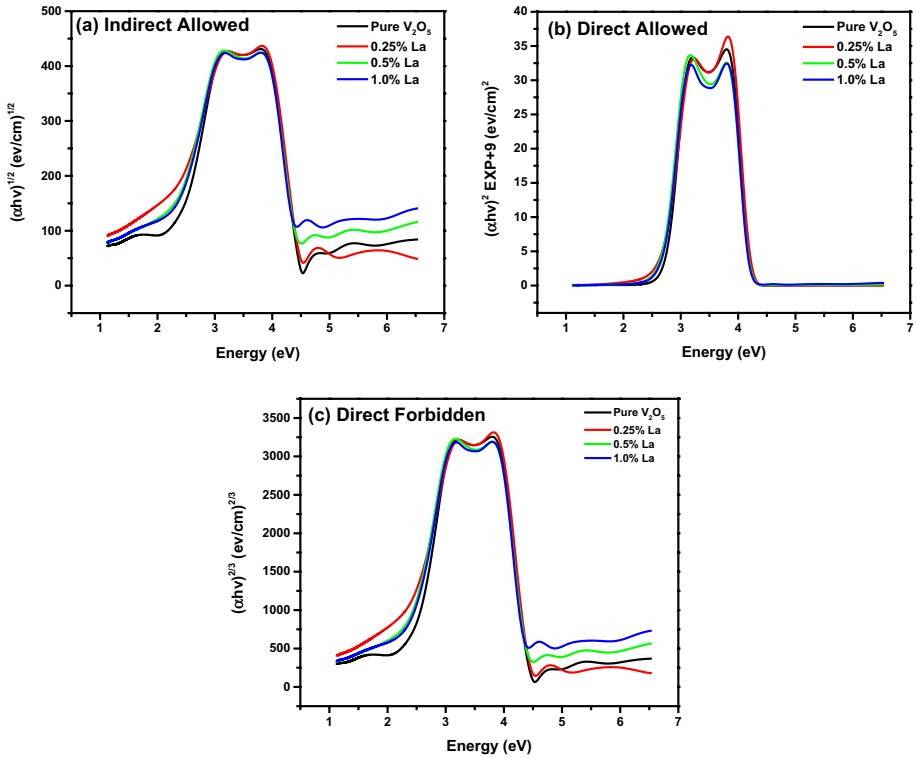
Fig. 18 **a** Indirect allowed band gap, **b** Direct allowed band gap, **c** Direct forbidden band gap

Table 3 Optical band gap for different contents of La oxide

La(mol%)	0%_Pure V_2O_5	0.25%	0.50%	1.0%
Indirect allowed band gap	2.28	2.02	2.14	2.16
Direct allowed band gap	2.74	2.68	2.68	2.69
Direct forbidden band gap	2.42	2.22	2.30	2.32

hand, m is related to the transition type where m = 2 for indirect allowed, m = 1/2 for direct allowed and m = 3/2 for direct forbidden.

Equation 14 can be re-written as following:

$$(\alpha h \upsilon)^{1/m} = \beta^{1/m} h \upsilon - E_{op} \tag{15}$$

where $\beta^{1/m}$ is constant. Now, to calculate the optical band gap, Eq. (15) is used. By plotting a graph between the energy in (eV) on the x-axis and $(\alpha h \upsilon)^{1/m}$ on Y-axis according to the type of the transition as following:

- $(\alpha h \upsilon)^{1/2}$ Vs. (hυ) → For indirect allowed band gap
- $(\alpha h \upsilon)^2$ Vs. (hυ) → For direct allowed band gap
- $(\alpha h \upsilon)^{2/3}$ Vs. (hυ) → For direct forbidden band gap

Table 4 Optical band gap average regression

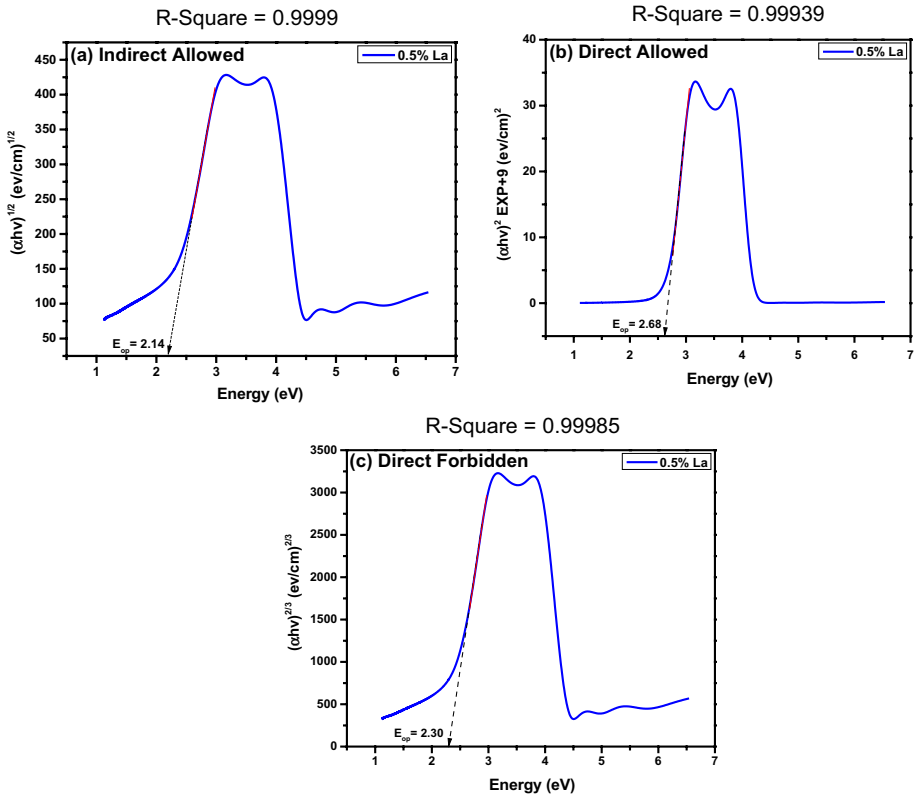| Transition type	Average regression "R"
Indirect allowed band gap	0.999**91**
Direct allowed band gap	0.999**39**
Direct forbidden band gap	0.999**89**

Fig. 19 Illustration for fitting to determine E_{op} for La $0.5V2O5.nH2O$

Figure 18a, b and c show the indirect allowed band gap, direct allowed band gap and direct forbidden band gap, respectively. From the graph, the linear portion of the curve is fitted for y-intersect which yields the band gap value, and slope of the fitted line, which gives the value of $\beta^{1/m}$. The obtained values for band gaps for different transition type are tabulated in Table 3. For determining the most suitable transition type, the regression coefficient for fixed number of fitted points was used (El-Desoky et al. 2020; Al-Assiri et al. 2010b). This is because all three optical transitions (forbidden and allowed) occur in thin films and the most transition type for V_2O_5 can vary due to impact from some factors like thin film preparation method, thin film thickness, type of substrate and UV irradiation (Schneider 2020). As illustrated in Table 4 for average

regression for various La contents, it was found that the indirect allowed band gap is the most suitable transition for prepared samples. Figure 19 illustrates the fitting for straight portion of the curve for 0.50%La for the various transition types as an example. Also, the band gap values for pure vanadium is close match to values obtained in previous studies (Dultsev et al. 2006; Tashtoush and Kasasbeh 2013).

The band gap for indirect allowed transition was found ranging from 2.02 to 2.28 eV with minimum value related to 0.25%La as illustrated in Fig. 20.

The variation in optical band gap associated with the addition of La oxide, can be attributed to the change in the absorption coefficient due to increasing of layers intercalating between V_2O_5 layers.

3.9 Urbach activation energy

In the low values of the absorption coefficient where $\alpha < 10^4$ cm.$^{-1}$, a small linear part appears generated from the localized states called the band tail. This region is related to low photon energy compared to optical band gap. Hence, it follows Urbach's rule (Mott and Davis 2012; Khan and Hogarth 1991). Equation (16), illustrates Urbach's rule where E_e is Urbach's energy and α_o is constant (Bahgat et al. 2005; Studenyak et al. 2014)

$$\alpha = \text{B} \ \exp \ \left(\text{hv}/\text{E}_e\right) \text{ for hv} < \text{E}_{op} \tag{16}$$

Generally, the Urbach energy represents the width of the localized states of the conduction band (band tail states).In other words, Urbach energy can be considered a numeric representation of the amount of damage caused by disorder in an amorphous or nanocrystalline semiconductor due to doping. The energy absorbed in this part is caused by optical transitions between localized states in the middle of the gap and extended states in the conduction or valence band plotting ln α as a function of $h\nu$, as shown in Fig. 21, by plotting ln (α) and the incident photon energy $(h\nu)$, a straight portion
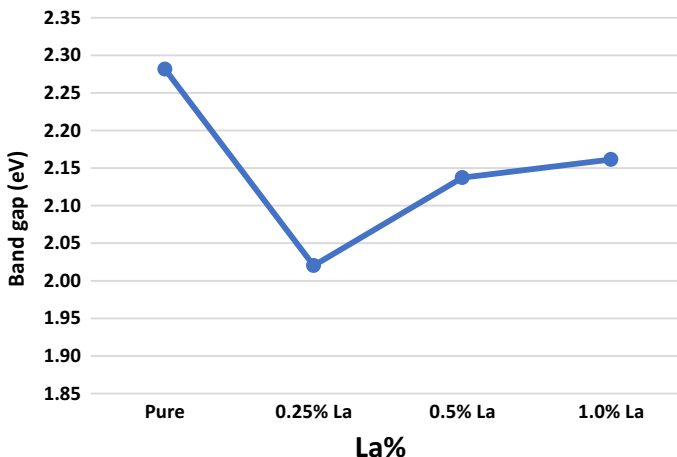

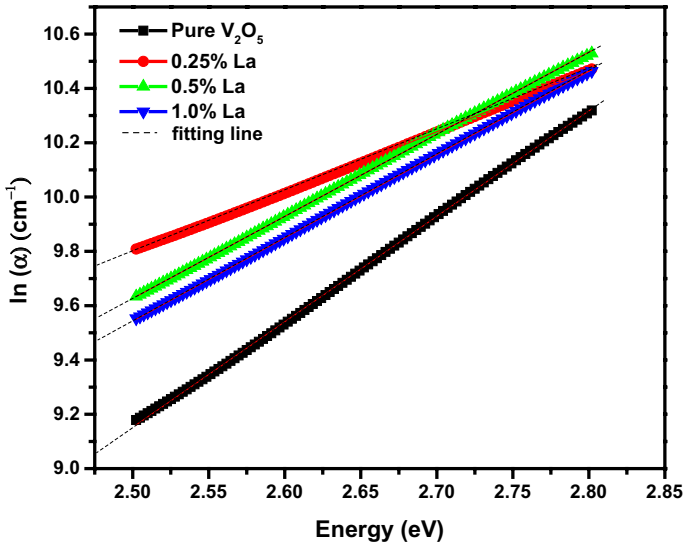**Fig. 20** The obtained results for E_{op} as a function of La content

Fig. 21 Urbach tail for different La content

Table 5 Urbach energy for different La oxide content

La(mol%)	0%_Pure	0.25%	0.50%	1.0%
Urbach Energy E_u (eV)	0.258	0.448	0.331	0.326

appears. The inverse slope of this line is the value of E_e (Morigaki and Ogihara 2017). The values were calculated and listed in Table 5 where it shows that Urbach energy has increased for 0.25%La relative to pure V_2O_5 sample and then decreased by increasing La content. This is an inverse relationship of Urbach tail energy with the band gap (Anyaegbunam and Augustine 2018).

3.9.1 Dispersion energy parameters

From the theory of classical dispersion, the spectral behavior of $n(\lambda)$ can be investigated using the model of single oscillator proposed by Wemple and Di-Domenico (WDD) (González-Leal 2013; Yakuphanoglu et al. 2004) as shown in Eq. (17)

$$n^2 = \frac{E_d E_o}{E_0^2 - (h\nu)^2} + 1 \tag{17}$$

where $E = h\nu$ is the incident photon energy, E_0 is the single-oscillator energy representing the average energy gap center-to-center of conduction to valence bands and E_d is the dispersion energy representing the oscillator strength which measures the strength of interband optical transitions.

Both E_o and E_d energy values can be calculated by modifying Eq. (17) as follows:
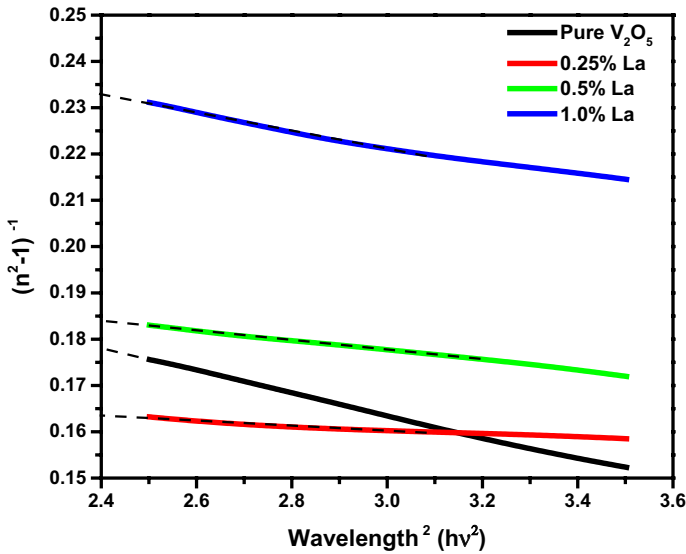
Fig. 22 Plotting $(n^2 - 1)^{-1}$ vs. $(h\nu)^2$ showing straight relation

$$(n^2 - 1)^{-1} = \frac{E_o}{E_d} - \frac{1}{E_o E_d}(h\nu)^2 \qquad (18)$$

Accordingly, by plotting $(n^2-1)^{-1}$ against $(h\nu)^2$ (as in Fig. 22) with linear fitting for straight portion, both E_o and E_d energies can be deduced as $(E_o E_d)^{-1}$ will be the slope and E_o / E_d is the y intercept of the straight fitted line.

Figure 22 shows the straight portion of $(n^2-1)^{-1}$ against $(h\nu)^2$ where the obtained values of E_o and E_d energies are listed in Table 6 where E_o can be correlated empirically to the band gap energy by the formula $E_o \approx 1.98\ E_{op}$ which is in good agreement with the empirical relation ($E_o \approx 2\ E_{op}$) proposed by Tanaka (Tanaka 1980).

Furthermore, the oscillator strengths f for transitions between valence and conduction bands, were calculated from the following equation (Wemple and DiDomenico 1971) and listed in Table 6:

$$f = E_o \times E_d \qquad (19)$$

Both dispersion energy E_d and oscillator strengths f have increased with the addition of La with maximum value for 0.25% La which can be furthermore investigated for optical communication applications.

The single-oscillator energy parameters E_o and E_d can also be used for the determination of imaginary dielectric constant moments M_1 and M_3 of the optical spectrum ($E_o^2 = \frac{M_1}{M_3}$ and $E_d^2 = \frac{M_1^3}{M_3}$) proposed by Wemple and Di-Domenico (Al-Assiri et al. 2010a; Nwofe et al. 2012). The M_1 and M_3 moments of the optical spectrum are listed in Table 6

Table 6 Dispersion energy parameters, effective mass and inter-atomic distance

La (mol%)	E_o (eV)	E_d (eV)	f $(eV)^2$	M_1	M_3	ε_∞	$N_t/m^* \times 10^{27}$	m^*/m_e	$N_t \times 10^{27}$ (m^{-3})	n_o	R (nm)
Pure V_2O_5	3.29	14.53	47.82	4.42	0.41	7.31	10.20	0.55	5.62	2.70	5.62
0.25% La	5.17	28.65	148.15	5.54	0.21	7.74	9.79	0.57	5.60	2.78	5.63
0.5% La	4.27	20.12	85.84	4.72	0.26	6.82	8.86	0.63	5.59	2.61	5.64
1.0% La	4.17	15.48	64.47	3.72	0.21	5.76	7.03	0.79	5.55	2.40	5.65

3.9.2 High-frequency dielectric constant and free charge carrier concentration

According to Pankove (Pankove 1971), the obtained values of refractive index n can be further used to calculate the high-frequency dielectric constant ε_∞ from the following equation

$$\varepsilon' = \varepsilon_\infty - \frac{e^2 N_t}{\pi \varepsilon_o m^* C^2} \lambda^2 \tag{20}$$

where ε_o is the lattice dielectric constant, λ is the wavelength, e is the electron charge, N_t is the free charge-carrier concentration, ε_o is the permittivity of the free space, m* is the effective mass in kg, and c is the speed of light.

By plotting the real dielectric constant ε' against the λ^2, a linear relations is noticed at higher wavelengths (Mady et al. 2012). Then, the linear fitting of this relation is extrapolated for y-axis intercept which equals to the value of ε_∞ as illustrated in Fig. 23. Moreover, the slope of this fitted line can be used to calculate the value of N_t/m^* (Abdel-Aziz et al. 2006). The obtained values of ε_∞ and N_t/m^* for the different La contents are listed in Table 6.

The optical relative dielectric permittivity n_o can now be calculated using the high-frequency dielectric constant ε_∞ using the following equation (Bahgat et al. 2008).

$$n_o = (\varepsilon_\infty)^{1/2} \tag{21}$$

The inter-atomic distance of the free charge carriers R, can be calculated using the following Eq. (22), (Al-Assiri et al. 2010b)
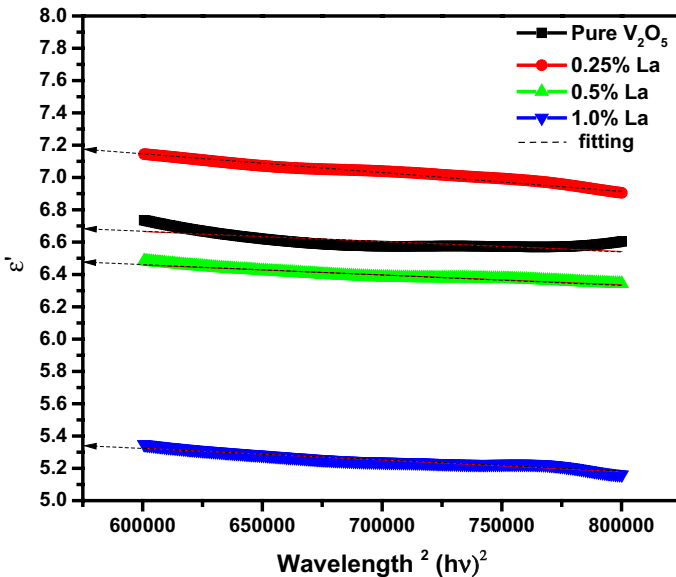
$$R = \frac{1}{N_t^{1/3}} \tag{22}$$

Fig. 23 Real part of the dielectric constant (ε') as a function of λ^2
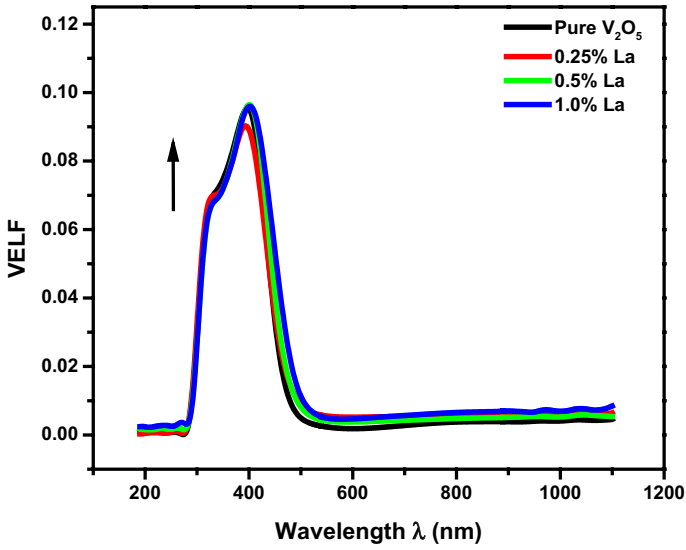
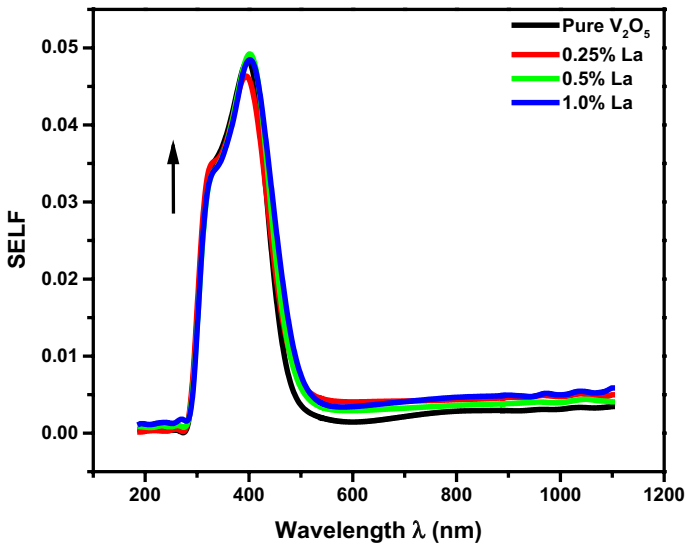**Fig. 24** Volume energy loss with La content

Fig. 25 Surface energy loss with La content

These optical parameters (N_t, n_o and R) are listed in Table 6.

3.9.3 The volume & surface energy loss functions

Volume energy loss function (VELF) parameter represents the electrons optical transition in bulk martial while surface energy loss function (SELF) parameter represents the electrons optical transition in thin films. VELF and SELF parameters were calculated using Eqs. (23) and (24), respectively (Ammar et al. 2002) and as illustrated in Figs. 24 and 25, respectively:

$$\text{VELF} = \varepsilon'' / \left(\varepsilon''^2 + \varepsilon'^2 \right) \tag{23}$$

$$\text{SELF} = \varepsilon'' / \left(\varepsilon''^2 + \left(\varepsilon' + 1 \right)^2 \right) \tag{24}$$

From the figures, it is clear that SELF values are much lower than VELF which can be attributed as most of the energy loss is resulting from inter-band electronic transition inside the nanocrystalline films compared to transition on its surface (Ali et al. 2013). Both (SELF) and (VELF) energy loss is decreasing by the addition of La.

4 Conclusion

Nanocrystalline thin films of $xLa_2O_3(x-1)nH_2OV_2O_5(0 \leq x \geq 1.0)$ were fabricated using the sol–gel method. XRD structural study revealed that the prepared samples are nanocrystalline with preferred orientation toward c-axis and particle size decreasing from 4.45 to 3.57 due to the addition of La content which increased the stress value from 36.9×10^{-3} to 52.93×10^{-3}. La content of 0.50% showed sharp peak of (002) which indicates to a critical concentration. Using spectroscopic study of absorbance, transmittance and reflectance of prepared films from 190 to 1100 nm wavelength, optical parameters such as absorption coefficient (α), absorptivity (â), extinction coefficient (k), real and imaginary dielectric constants, transition type, optical band gap (E_{op}), Urbach tail energy (E_e) dissipation factor (tan δ), volume (VELF) and surface (SELF) energy loss functions were calculated. The absorptivity (â) for visible spectrum was enhanced for 0.50%La sample which is promising for solar energy applications. Dispersion energy parameters were studied using Wemple – Didomenico single effective oscillator model. Relating the real part of the optical dielectric function led to the calculation of the charge carrier concentration and their effective mass. The change of optical parameters such as n, k, E_{op}, E_e, E_o, E_d, SELF and VELF is directly related to the increasing amounts of lanthanum doping.

Declarations

Competing interests The authors declare that they have no known competing financial interests or personal relationships that could have appeared to influence the work reported in this paper.

Ethical approval Not applicable.

References

Abdel-Aziz, M., Yahia, I., Wahab, L., Fadel, M., Afifi, M.: Determination and analysis of dispersive optical constant of TiO_2 and Ti_2O_3 thin films. Appl. Surf. Sci. **252**(23), 8163–8170 (2006)

Abyazisani, M., Bagheri-Mohagheghi, M.M., Benam, M.R.: Study of structural and optical properties of nanostructured V_2O_5 thin films doped with fluorine. Mater. Sci. Semicond. Process. **31**, 693–699 (2015)

Al-Assiri, M., El-Desoky, M., Alyamani, A., Al-Hajry, A., Al-Mogeeth, A., Bahgat, A.: Spectroscopic study of nanocrystalline $V_2O_5 \cdot nH_2O$ films doped with Li ions. Opt. Laser Technol. **42**(6), 994–1003 (2010a)

Al-Assiri, M., et al.: Spectroscopic study of nanocrystalline $V_2O_5 \cdot nH_2O$ films doped with Li ions. J. Opt. **42**(6), 994–1003 (2010b)

Ali, A., Son, J., Ammar, A., Moez, A.A., Kim, Y.: Optical and dielectric results of $Y_0.225Sr_0.775CoO_3 \pm \delta$ thin films studied by spectroscopic ellipsometry technique. Results Phys. **3**, 167–172 (2013)

Al-Qaisi, B.: UV spectroscopy, refractive indices and elastic properties of the (76–x) $TeO_2 \cdot 9P_2O_5 \cdot 15ZnO \cdot xLiNbO_3$ glass. Solid State Sci. **19**, 6–11 (2013)

Amlouk, A., Boubaker, K., Amlouk, M., Bouhafs, M.: Study of ytterbium doping effects on structural, mechanical and opto-thermal properties of sprayed ZnO thin films using the boubaker polynomials expansion scheme (BPES). J. Alloys Compd. **485**(1–2), 887–891 (2009)

Ammar, A., El-Sayed, B., El-Sayad, E.: Structural and optical studies on ortho-hydroxy acetophenone azine thin films. J. Mater. Sci. **37**(15), 3255–3260 (2002)

Annapoorani, K., Suriya-Murthy, N., Ravindran, T.R., Marimuthu, K.: Influence of Er^{3+} ion concentration on spectroscopic properties and luminescence behavior in Er^{3+} doped Strontium telluroborate glasses. J. Lumin. **171**, 19–26 (2016)

Anyaegbunam, F.N.C., Augustine, C.: A study of optical band gap and associated urbach energy tail of chemically deposited metal oxides binary thin films. Dig. J. Nanomater. Biostruct. **3**(3), 847–856 (2018)

Arefinia, Z., Asgari, A.: Novel attributes in the scaling and performance considerations of the one-dimensional graphene-based photonic crystals for terahertz applications. Phys. E **54**, 34–39 (2013)

Aristizábal, A., Mikan, M.: Optical properties of CDS films by analysis of spectral transmittance. IOSR J. Appl. Phys. **8**(4), 24–31 (2016)

Bahgat, A., Ibrahim, F., El-Desoky, M.: Electrical and optical properties of highly oriented nanocrystalline vanadium pentoxide. Thin Solid Films **489**(1–2), 68–73 (2005)

Bahgat, A.A., Abd Rabo, A.S., Mahdy, I.A., Mahmoud, E.A.: Spectral features of $Ge_{50} - ySbxTe_{50} - x + y$ alloys where $0 \leqslant x \leqslant 15$ and $0 \leqslant y \leqslant 30$ in thin film state. Opt. Laser Technol. **40**(8), 1061–1067 (2008)

Bahgat A., Ibrahim F. El-Desoky M.: Nanocrystalline vanadium pentoxide xerogel properties and hydrogen sensing. In: AIP Conference Proceedings, vol. 1370, pp. 61–67. AIP (2011)

Caglar, M., Caglar, Y., Ilican, S.: The determination of the thickness and optical constants of the ZnO crystalline thin film by using envelope method. J. Optoelectron. Adv. Mater. **8**(4), 1410–1413 (2006)

Chikhale, L.P., Patil, J.Y., Rajgure, A.V., Shaikh, F.I., Mulla, I.S., Suryavanshi, S.S.: Structural, morphological and gas sensing properties of undoped and Lanthanum doped nanocrystalline SnO_2. Ceram. Int. **40**(1), 2179–2186 (2014)

Dultsev, F., Vasilieva, L., Maroshina, S., Pokrovsky, L.: Structural and optical properties of vanadium pentoxide sol–gel films. Thin Solid Films **510**(1–2), 255–259 (2006)

El-Desoky, M.M., Ali, M.A., Afifi, G., Imam, H.: Annealing effects on the structural and optical properties of growth ZnO thin films fabricated by pulsed laser deposition (PLD). J. Mater. Sci. Mater. Electron. **25**, 5071–5077 (2014)

El-Desoky, M.M., El-Barbary, G.A., El Refaey, D.E., El-Tantawy, F.: Optical constants and dispersion parameters of La-doped ZnS nanocrystalline films prepared by sol–gel technique. Optik **168**, 764–777 (2018)

El-Desoky, M.M., Abdulrazek, M.M., Sharaby, Y.A.: Characterization and optical properties of reduced graphene oxide doped nano-crystalline vanadium pentoxide. Opt. Quantum Electron. **52**(6), 315–342 (2020)

El-Nahhas, M., Abdel-Khalek, H., Salem, E.: Optical properties of 3, 4, 9, 10-perylenetetracarboxylic diimide (PTCDI) organic thin films as a function of post-annealing temperatures. Am. J. Mater. Sci. **2**(4), 131–137 (2012)

Etemadi, B., Mazloom, J., Ghodsi, F.E.: Phase transition and surface morphology effects on optical, electrical and lithiation/delithiation behavior of nanostructured Ce-doped V_2O_5 thin films. Mater. Sci. Semicond. Process. **61**, 99–106 (2017)

Fang, D., et al.: Influence of Al doping on structural and optical properties of Mg–Al co-doped ZnO thin films prepared by sol–gel method. J. Alloys Compd. **589**, 346–352 (2014)

Ghobadi, N.: Band gap determination using absorption spectrum fitting procedure. Int. Nano Lett. **3**(1), 2–5 (2013)

González-Leal, J.: The Wemple–DiDomenico model as a tool to probe the building blocks conforming a glass. Phys. Status Solidi (B) **250**(5), 1044–1051 (2013)

Indolia, A.P., Gaur, M.S.: Optical properties of solution grown PVDF-ZnO nanocomposite thin films. J. Polym. Res. **20**, 1–8 (2013)

Islam, M.R., Podder, J.: Optical properties of ZnO nano fiber thin films grown by spray pyrolysis of zinc acetate precursor. Cryst. Res. Technol. J. Exp. Ind. Crystallogr. **44**(3), 286–292 (2009)

Kaelble, E.F.: Handbook of X-rays: for Diffraction, Emission, Absorption, and Microscopy. McGraw-Hill, New York (1967)

Khan, G., Hogarth, C.: Optical absorption spectra of evaporated V_2O_5 and co-evaporated V_2O_5/B_2O_3 thin films. J. Mater. Sci. **26**(2), 412–416 (1991)

Klein, L.C.: Sol-gel Optics: Processing and Applications. Springer, Cham (2013)

Lazzez, S., Mahmoud, K.B.B., Abroug, S., Saadallah, F., Amlouk, M.: A Boubaker polynomials expansion scheme (BPES)-related protocol for measuring sprayed thin films thermal characteristics. Curr. Appl. Phys. **9**(5), 1129–1133 (2009)

Lee, S.-W., et al.: UV degradation and recovery of perovskite solar cells. Sci. Rep. **6**, 38150–38155 (2016)

Legendre, J.-J., Aldebert, P., Baffier, N., Livage, J.: Vanadium pentoxide gels: II. Structural study by x-ray diffraction. J. Colloid Interface Sci. **94**, 84–89 (1983)

Li, L., et al.: The determination of the thickness and optical constants of the microcrystalline silicon thin film by using envelope method. Optoelectron. Adv. Mater. Rapid Commun. **3**(6), 625–630 (2009)

Li, Z., Sun, H., Xu, J., Zhu, Q., Chen, W., Zakharova, G.S.: The synthesis, characterization and electrochemical properties of $V_3O_7 \cdot H_2O$/CNT nanocomposite. Solid State Ion. **262**, 30–34 (2014)

Lozano, W., de Araújo, C.B., Ledemi, Y., Messaddeq, Y.: Upconversion luminescence in Er^{3+} doped $Ga_{10}Ge_{25}S_{65}$ glass and glass-ceramic excited in the near-infrared. J. Appl. Phys. **113**(8), 083520–083525 (2013)

Maaoui, A., Ben Slimen, F., Haouari, M., Bulou, A., Boulard, B., Ben Ouada, H.: Upconversion and near infrared emission properties of a novel Er^{3+}/Yb^{3+} codoped fluoro-tellurite glass. J. Alloys Compd. **682**, 115–123 (2016)

Mady, H.A., Negm, S.E., Moghny, A.A., Abd-Rabo, A., Bahgat, A.: Study of optical properties of highly oriented nanocrystalline $V_2O_5 \cdot nH_2O$ films doped with K ions. J. sol-gel Sci. Technol. **62**(1), 18–23 (2012)

Maheshvaran, K., Arunkumar, S., Venkata-Krishnaiah, K., Marimuthu, K.: Investigations on luminescence behavior of Er^{3+}/Yb^{3+} co-doped boro-tellurite glasses. J. Mol. Struct. **1079**, 130–138 (2015)

Mahmoud, K.B.B., Amlouk, M.: The 3D Amlouk-Boubaker expansivity–energy gap–Vickers hardness abacus: a new tool for optimizing semiconductor thin film materials. Mater. Lett. **63**(12), 991–994 (2009)

Maqbool, M., Ahmad, I., Ali, G., Maaz, K.: Energy level splitting and luminescence enhancement in AlN: Er by an external magnetic field. Opt. Mater. **46**, 601–604 (2015)

Matkovic, A., Gajic, R.J.S.N.: Spectroscopic imaging ellipsometry of graphene. SPIE Newsroom **45**, 4561–4564 (2013). https://doi.org/10.1117/2.1201311.005227

Mohaghegh, Z., Ghodsi, F.E., Mazloom, J.: Comparative study of electrical parameters and Li-ion storage capacity of PEG modified β-V_2O_5: M (M: Mo, Ni) thin films. J. Mater. Sci. Mater. Electron. **30**, 13582–13592 (2019)

Mohanty, D.K., Rai, V.K.: Spectroscopy and visible frequency upconversion in Er^{3+}–Yb^{3+}: TeO_2–ZnO glass. Spectrochim. Acta Part A Mol. Biomol. Spectrosc. **121**, 9–13 (2014)

Monteiro, G., Li, Y., Santos, L.F., Almeida, R.M.: Optical and spectroscopic properties of rare earth-doped (80–x)TeO_2–$xGeO_2$–$10Nb_2O_5$–$10K_2O$ glasses. J. Lumin. **134**, 284–296 (2013)

Morigaki, K., Ogihara, C.: Amorphous semiconductors: structure, optical, and electrical properties. In: Springer Handbook of Electronic and Photonic Materials, pp. 1–1. Springer, Cham (2017)

Mott, N.F., Davis, E.A.: Electronic Processes in Non-Crystalline Materials. Oxford University Press, Oxford (2012)

Mrabet, C., Boukhachem, A., Amlouk, M., Manoubi, T.: Improvement of the optoelectronic properties of tin oxide transparent conductive thin films through lanthanum doping. J. Alloys Compd. **666**, 392–405 (2016)

Nagaraju, D.H., Wang, Q., Beaujuge, P., Alshareef, H.N.: Two-dimensional heterostructures of V_2O_5 and reduced graphene oxide as electrodes for high energy density asymmetric supercapacitors. J. Mater. Chem. A **2**(40), 17146–17152 (2014)

Nwofe, P., Reddy, K.R., Tan, J., Forbes, I., Miles, R.: Thickness dependent optical properties of thermally evaporated SnS thin films. Phys. Procedia **25**, 150–157 (2012)

Pankove, J.: Absorption. In: Optical Processes in Semiconductors: Prentice-Hall, pp. 34–86. Inc Englewood Cliffs, New Jersey (1971)

Prociow, E., Zielinski, M., Sieradzka, K., Domaradzki, J., Kaczmarek, D.: Electrical and optical study of transparent V-based oxide semiconductors prepared by magnetron sputtering under different conditions. Radioengineering **20**(1), 204–208 (2011)

Ramana, C., Hussain, O., Naidu, B.S., Reddy, P.: Spectroscopic characterization of electron-beam evaporated V_2O_5 thin films. Thin Solid Films **305**(1–2), 219–226 (1997)

Roose, B., et al.: Mesoporous SnO_2 electron selective contact enables UV-stable perovskite solar cells. Nano Energy **30**, 517–522 (2016)

Roose, B., et al.: A Ga-doped SnO_2 mesoporous contact for UV stable highly efficient perovskite solar cells. J. Mater. Chem. A **6**(4), 1850–1857 (2018)

Sajna, M.S., Thomas, S., Ann-Mary, K.A., Joseph, C., Biju, P.R., Unnikrishnan, N.V.: Spectroscopic properties of Er^{3+} ions in multicomponent tellurite glasses. J. Lumin. **159**, 55–65 (2015)

Sánchez-González, J., Díaz-Parralejo, A., Ortiz, A., Guiberteau, F.: Determination of optical properties in nanostructured thin films using the Swanepoel method. Appl. Surf. Sci. **252**(17), 6013–6017 (2006)

Schmiedova, V., et al.: Physical properties investigation of reduced graphene oxide thin films prepared by material inkjet printing. J. Nanomater. **2017**, 1–8 (2017). https://doi.org/10.1155/2017/3501903

Schneider, K.: Optical properties and electronic structure of V_2O_5, V_2O_3 and VO_2. J. Mater. Sci. Mater. Electron. **31**(13), 10478–10488 (2020)

Seshadri, M., Chillcce, E.F., Marconi, J.D., Sigoli, F.A., Ratnakaram, Y.C., Barbosa, L.C.: Optical characterization, infrared emission and visible up-conversion in Er^{3+} doped tellurite glasses. J. Noncryst. Solids **402**, 141–148 (2014)

Srilakshmi, P., Maheswari, A.U., Sajeev, V., Sivakumar, M.: Tuning the optical bandgap of V_2O_5 nanoparticles by doping transition metal ions. Mater. Today Proc. **18**, 1375–1379 (2019)

Studenyak, I., Kranjčec, M., Kurik, M.: Urbach rule in solid state physics. Int. J. Opt. Appl. **4**(3), 96–104 (2014)

Takeda, S., et al.: Structure and dynamical properties of molten V_2O_5. J. Noncryst. Solids **205**, 151–154 (1996)

Tanaka, K.: Optical properties and photoinduced changes in amorphous as S films. Thin Solid Films **66**(3), 271–279 (1980)

Tashtoush, N.M., Kasasbeh, O.: Optical properties of vanadium pentoxide thin films prepared by thermal evaporation method. Deanship of Scientific Research and Graduate Studies, Wuhan 7–15 (2013)

Wemple, S.H., DiDomenico, M., Jr.: Behavior of the electronic dielectric constant in covalent and ionic materials. Phys. Rev. B **3**(4), 1338 (1971)

Wright, A.C.: The structure of vitreous and liquid V_2O_5. Philos. Mag. B **50**(3), L23–L28 (1984)

Yakuphanoglu, F., Cukurovali, A., Yilmaz, I.: Single-oscillator model and determination of optical constants of some optical thin film materials. Phys. B **353**, 210–216 (2004). https://doi.org/10.1016/j.physb.2004.09.097

Yao, T., Oka, Y.: On the layer structure of vanadium pentoxide gels comment on "molecular dynamic simulation of the vanadium pentoxide gel host." Solid State Ion. **96**(3–4), 127–128 (1997)

Zhao, Z., Lin, X., Dai, Y.: Lanthanum-containing catalytic materials and their applications in heterogeneous catalysis. Chem. Inform. (2011). https://doi.org/10.1002/chin.201136216